Patterned Electroconvective States in a Bent-Core Nematic Liquid Crystal

4 AUTHORS:

Pramod Tadapatri
Raman Research Institute
9 PUBLICATIONS   **76** CITATIONS

SEE PROFILE

Uma Hiremath
Centre for Nano and Soft Matter Sciences
52 PUBLICATIONS   **597** CITATIONS

SEE PROFILE

C. V. Yelamaggad
Centre for Nano and Soft Matter Sciences
165 PUBLICATIONS   **2,083** CITATIONS

SEE PROFILE

K. S. - Krishnamurthy
Centre for Nano and Soft Matter Sciences (…
41 PUBLICATIONS   **239** CITATIONS

SEE PROFILE

Patterned Electroconvective States in a Bent-Core Nematic Liquid Crystal

Pramod Tadapatri, Uma S. Hiremath, C. V. Yelamaggad, and K. S. Krishnamurthy*

Centre for Liquid Crystal Research, P.O. Box 1329, Jalahalli, Bangalore 560 013, India

We report the results of investigations on the anisotropic electrohydrodynamic states arising in a highly conducting, planarly aligned, bent-core nematic liquid crystal driven by ac fields of frequency f in the range from 10 Hz to 1 MHz. Pattern morphologywise, two f regimes are distinguished. The low-f regime, wherein the primary bifurcation is to a state of periodic longitudinal stripes (LS), extends to an unprecedentedly large f, in the range 150−550 kHz, depending on the temperature T. This is followed by the high-f regime wherein periodic normal stripes (NS) constitute the primary instability. Both instabilities involve predominant director modulations and streamlines in the layer plane. The transitional frequency between the two regimes is linear in temperature. The curve $V_c(f)$ shows a nonlinear increase for the LS state and decrease for the NS state. $V_c(T)$ is an ever increasing curve close to the nematic−isotropic point for both states. The wavenumber of LS varies directly as V, and that of NS shows nearly the same behavior. The pattern period versus f is increasing for LS but decreasing for NS. Both instability states exhibit complex, light-polarization-dependent lens action. Well above the threshold, disclination loops of regular geometry appear along the stripes. They drift in a coordinated manner along the flow lines. At very high voltages, the instability turns strongly time dependent. The current models of anisotropic convection based on static electrical parameters fail to account for the observed instabilities.

1. Introduction

Nematic liquid crystals are among the best known nonequilibrium pattern-forming systems. Bifurcation of the rest state of uniform alignment into an electroconvective patterned state in a nematic is often driven by the Carr−Helfrich (CH) mechanism.[1−3] For a planarly oriented sample with the director $\mathbf{n}_o = (1, 0, 0)$, in a static field $\mathbf{E} = (0, 0, E)$, the one-dimensional (1D) CH analysis of the coupling between electrical conductivity anisotropy and the bend curvature distortion leads to formation of periodic space charges of alternating sign along the alignment direction, x. The body force on these charges sets up periodic cellular flows above a critical voltage V_c determined by the balance between hydrodynamic, dielectric and elastic torques. The corresponding analysis for an ac field[4] reveals the existence of a cutoff frequency f_c separating two regimes of instability: In the conduction regime, below f_c, the space charges oscillate at the field frequency while the director pattern remains static; beyond f_c, in the dielectric regime, the space charges are almost static but the director oscillates. A three-dimensional generalization of the CH theory, referred to as the standard model (SM),[5,6] captures many of the threshold features of anisotropic nematic electroconvection (EC) such as the frequency dependence of the tilt of convective rolls, threshold voltage, and critical wavenumber of the roll pattern. According to the SM, for an initially planar sample and frequency $f < f_c$, the threshold voltage V_o appropriate to the wave vector $\mathbf{k} = (q, p)$ is given by

$$V_o^2 = \frac{\pi^2 k^*}{\varepsilon_o \varepsilon_a^* - \dfrac{\sigma_a^* \tau \alpha_2}{\eta^*}} \tag{1}$$
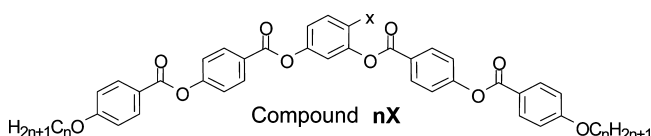
with

$$\tau = \frac{\varepsilon_o \varepsilon_\perp}{\sigma_\perp}, \varepsilon_a = (\varepsilon_\parallel - \varepsilon_\perp), \sigma_a = (\sigma_\parallel - \sigma_\perp)$$

Here the asterisk (*) signifies the effective value of the corresponding material parameter, k, ε_a, σ_a, and η denote, respectively, the elastic modulus, dielectric anisotropy, conductivity anisotropy, and viscosity coefficient, τ is the charge relaxation time, α_2 is a Leslie viscosity coefficient, and the subscripts ‖ and ⊥ specify the directions relative to initial director $\mathbf{n}_o$. While all the starred quantities involve the components of $\mathbf{k}$, the electrical anisotropies depend additionally on the field frequency. Above a frequency f_L, the so-called Lifshitz point, the threshold pattern consists of normal rolls (NRs) perpendicular to the x axis with the minimum of the neutral curve $V_o(q, p = 0)$ occurring at the absolute or critical threshold V_c and wavenumber q_c; oblique rolls (ORs) form below f_L, where $p_c > 0$ yields a lower threshold. Beyond f_c, the instability consists of dielectric rolls (DRs)[7] that manifest optically as close-spaced (wavelength, $\lambda <$ sample thickness, d) normal stripes at V_c and as chevron-like oblique stripes above V_c.

Much of our understanding of anisotropic electroconvection in uniaxial nematics is derived almost exclusively from experiments with rod-like or calamitic mesogens. In fact, rod-like nematics with negative ε_a, positive σ_a, and planar initial alignment p, referred to conveniently as (− + p) materials, are established to be ideal candidates for displaying, in the conduction regime, the so-called standard electroconvection; it consists of a well-ordered sequence of CH instabilities that evolve with increasing control parameter, starting with periodic rolls at V_c and developing into chaotic flows far from equilibrium, at $\sim 2V_c$.[8] In recent years, there have been several studies on calamitics with other combinations of initial texture (planar p, homeotropic h or tilted t) and signs of ε_a and σ_a.[9−14] Thus, several electrohydrodynamic structures that do not conform to the SM have come to light, and they are often described as

* To whom correspondence should be addressed. E-mail: murthyksk@gmail.com.

Patterned Electroconvective States

J. Phys. Chem. B, Vol. 114, No. 1, 2010 **11**

belonging to nonstandard electroconvection (NSEC).[10] There have been some recent theoretical advances that incorporate flexoelectric effects in the SM to account for some of the nonstandard features of EC.[13,14]

By far, electric-field-generated patterned states in nematic liquid crystals formed of bent-core (BC) molecules have received a limited attention:[15–21] A few of the reports on the syntheses of several BC compounds belonging to the series **nX** with **X** = Cl, Br, or CN deal very briefly with some unusual electrooptic effects in these compounds: Under an increasing dc or low-frequency field, planar nematic samples of **nCl**[15,16] and **nCN**[17] exhibit in succession striped patterns, myelinic domains, and smectic-like fan textures; in **nBr**,[16] under ac excitation, broad stripe domains form transverse to the initial alignment direction.


Recently, Wiant et al.[18] performed a detailed investigation of electroconvection in nematic layers of 4-chloro-1,3-phenylene bis-4-[4′-(9-decenyloxy)benzoyloxy]benzoate (compound **1**) with the initial planar orientation of the director. The voltage–frequency (V–f) plane for this (− ± p) nematic reveals the existence of three electroconvective regimes which, in the order of their occurrence with increasing *f*, are the parallel stripes (PS), prewavy 2 (PW2), and PW1 states; between the two PW states, which are characterized optically by periodic stripes normal to the director, there exists an empty region (ER) devoid of any instability. None of the three instabilities finds an explanation within the framework of the SM.
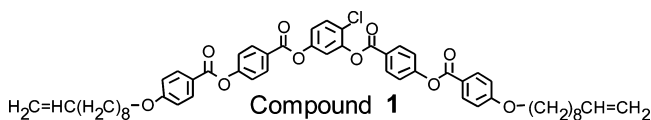

In a subsequent study, Tanaka et al.[19] found a slightly different EC scenario in the (− −) nematic naphthalene-2,7-diyl bis(3-fluoro-4-(2-methyl-3-(4-(tetradecyloxy)phenyl) acryloyloxy)benzoate) (compound **2**). The phase diagram of **2** shows PW2 and PW1 regions as in **1**, but they are separated by an ill-defined patterned state instead of the ER. More importantly, on rotation of the sample between crossed polarizers, the PW stripes show no extinction for any orientation. This is interpreted as indicative

of a twisted structure such as found in surface stabilized ferroelectric liquid crystal cells.
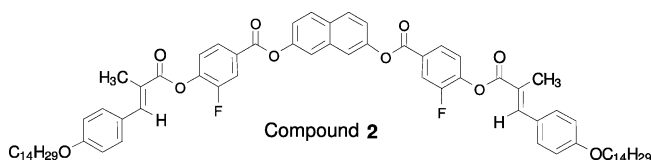
Very recently, Tanaka et al.[20] investigated electroconvection in binary mixtures of compound **1** and a calamitic nematic liquid crystal and found for the BC-rich mixtures the same sequence of instabilities as for the pure BC component. In another study, Xiang et al.[21] report the distinctive voltage–temperature phase diagrams of the uniaxial and biaxial nematic phases in compound **3** and interpret their observations through changes in electrical conductivity anisotropy at the uniaxial to biaxial transition.
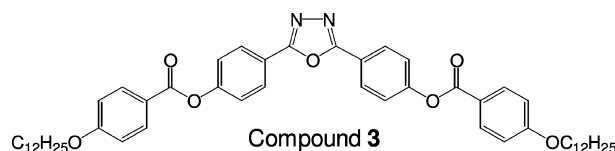
There have also been some recent studies on electroconvective secondary instabilities evolving from the bend and splay Freedericksz states in a couple of bent-rod nematic liquid crystals.[22–25] Conventional NRs, broad PW-like domains, defect-free chevrons (DFCs), defect-mediated chevrons (DMCs), and time-dependent states have all been observed under various excitation conditions in 4-((3-(4-(4-(decyloxy)benzoyloxy)benzoyloxy)phenylimino)-methyl)-3-hydroxyphenyl 4-(6-(4′-cyanobiphenyl-4-yloxy)hexyl-oxy)benzoate (compound **3**); the material, taken initially in the (+ + h) state, is examined beyond the dielectric inversion frequency. Significantly, all the observed periodic states exhibit the phase propagation phenomenon.[22,23] Another bent-rod material, compound **4**, belonging to the (+ −) category and planarly oriented to start with, is reported[24,25] to bifurcate from the homogeneous splay distorted state into a convective roll state at a threshold voltage that increases monotonically with frequency; with rising *f*, there occurs a succession of patterned states corresponding to longitudinal, zigzag (oblique), normal, and fluctuating convection rolls, all of which are thought to be explicable through an adaptation of the CH mechanism involving a periodic twist modulation superimposed on a homogeneous splay; further, voltage-dependent longitudinal-to-normal rolls transformation is detected in a metastable phase, conjectured as a biaxial nematic phase obtained through aging of the uniaxial N phase in high electric fields.
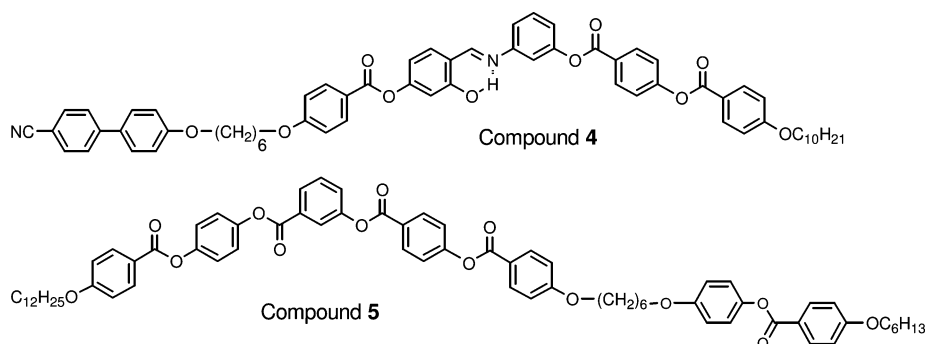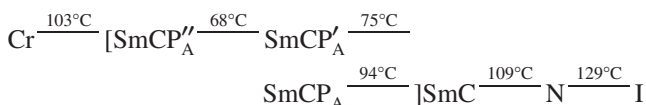
TABLE 1: Some Material Parameters of Relevance to Electroconvection

T^*	$\varepsilon_\|$	$\varepsilon_\perp$	$\sigma_\|$ (μS m^{-1})	$\sigma_\perp$ (μS m^{-1})	k_{11} (pN)	k_{33} (pN)	γ_1 (Pa s)	γ_{1a} (Pa s)
0.9623	7.24	10.24	0.209	0.350	18.4	4.2	2.2	6.9

The present investigation concerns the electroconvective states in the BC material 4-cyanoresorcinol bis[4-(4-*n*-dodecyloxy-benzoyloxy)benzoate] (**CNRbis12OBB**) belonging to the **nCN** series referred to earlier. The instability scenario for this compound is in some ways different from that for either compound **1** or **2**. It is our purpose here to characterize in detail the patterned states observed over a wide frequency band extending to 1 MHz and discuss them comparatively with the results for other BC systems.

2. Experimental Methods

Kovalenko et al.[17] were the first to synthesize **CNRbis12OBB** and report its phase sequence as

$$\text{Cr} \xrightarrow{103°C} [\text{SmCP}''_A \xrightarrow{68°C} \text{SmCP}'_A \xrightarrow{75°C}$$

$$\text{SmCP}_A \xrightarrow{94°C}]\text{SmC} \xrightarrow{109°C} \text{N} \xrightarrow{129°C} \text{I}$$

with Cr, SmCP$_A$, SmC, N, and I denoting, respectively the crystal, antipolar smectic C, smectic C, nematic, and isotropic phases. The nematic phase in virgin samples of **CNRbis12OBB** synthesized by us had a clearing temperature T_{NI} of 128.5 °C; during continued electric field experiments, it dropped to a minimum of ~125 °C, while the N range remained about 20 °C. We indicate the temperature here by its reduced value $T^* = T/T_{NI}$, with T and T_{NI} in Kelvin.

The sample cells used were sandwich type, constructed of passivated, indium tin oxide (ITO) coated glass plates from Delta Technologies. The planar alignment was secured by spin coating the ITO electrodes with polyimide and then buffing unidirectionally the coated surfaces on velvet cloth. The rubbing direction and layer normal define the reference axes x and z, respectively. Mylar spacers, heat sealed to the electrodes through cooling from ~ 250 °C under a uniform pressure, determined the cell gap d; d was measured interferometrically. For optical observations, a Carl-Zeiss Axio Imager.M1m polarizing microscope equipped with an AxioCam MRc5 digital camera was used. The sample temperature T was maintained to an accuracy of ±0.1 °C by an Instec HCS402 hot-stage connected to a STC200 temperature controller. The voltage source was a Stanford Research Systems DS345 function generator coupled to a FLC Electronics voltage amplifier (model A800). The applied voltage, V, was measured with a Keithley-200 multimeter.

We have also measured various material parameters of relevance to electroconvection and reported our results in a separate communication.[26] It is necessary to note here a few of the important results: The permittivity anisotropy ε_a is negative in the entire N range; its value measured at 1 kHz varies between 3.546 at $T^* = 0.9547$ and 0.689 at $T^* = 0.9949$. The conductivity anisotropy σ_a is negative at low frequencies; its value for 1 kHz varies between 0.140 μS m^{-1} at $T^* = 0.9547$ and 0.048 μS m^{-1} at $T^* = 0.9949$. Some representative values of the measured physical constants are presented in Table 1, where the electrical parameters are for 1 kHz and γ_1 and γ_{1a} are the rotational viscosity coefficients corresponding to a two-step relaxation process.

Above a few kHz, $\sigma_a(f)$ becomes dynamic. The sign of σ_a changes twice at f_1 and f_2, being positive between these crossover frequencies. The temperature variation of f_1 and f_2 is shown in Table 2.

TABLE 2: Temperature Dependence of σ_a Sign Reversal Points

T^*	f_1 (kHz)	f_2 (kHz)
0.9548	6.7	80
0.9623	7.8	117
0.9749	9.3	218
0.9874	9.9	392
0.9949	10.2	570

3. Results and Discussion

3.1. Electric-Field-Induced Patterned States. In the description of the patterns to follow, we indicate the setting of the polarizer P and analyzer A by P(β)−A(β'), where β and β' are the angles in degrees made by the corresponding transmission axes with the initial alignment direction x. Voltage amplitudes specified are the rms values, the applied voltage being $V(t) = \sqrt{2}\, V_{rms} \sin \omega t$.

We present in Figure 1 the phase diagram of **CNRbis12OBB** showing the frequency dependence of the critical voltage V_c at which the patterned states optically manifest. The primary instabilities occurring over a wide range of f (from 10 Hz to 1 MHz) constitute two distinct regimes: The low-frequency regime of longitudinal stripes (LS) and the high-frequency regime of normal stripes (NS).

Longitudinal Stripes Instability. These stripes extend predominantly along $\mathbf{n}_o$, with the effective wave vector $\mathbf{k} \perp \mathbf{n}_o$ and possess a threshold period 2d-3d. For bent-core systems, such a texture of broad bands occurring over a very wide frequency range at the primary bifurcation from the rest state has, to the best of our knowledge, not been reported until now, although a similar instability has been noticed at a secondary bifurcation from the splay-Freedericksz base state.[24,25] For constant d and T, the optical threshold of the LS increases with f, and very broadly three linear sections of $V_c(f)$ are recognizable; in the first 10 kHz the average slope of $V_c(f)$ is the highest; then up to ~100 kHz it is the lowest; beyond this frequency and up to what may be called the cutoff frequency f_{LN} it is intermediate. Above f_{LN}, the primary instability that occurs is the NS state discussed later.

We illustrate in Figure 2 the typical near-threshold appearance of the LS under white light illumination. The texture in Figure 2a for crossed polarizers P(0)−A(90) shows periodic extinction of light along slightly wavy lines, with colored bands appearing
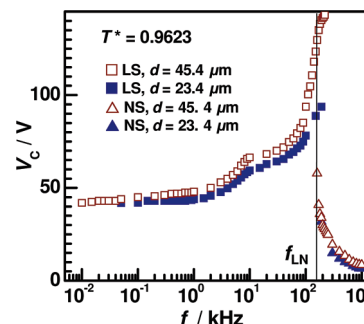

Figure 1. Frequency dependence of the optical threshold V_c at which the primary bifurcation into a patterned state is observed at $T^* = 0.9623$ (110 °C) in samples of two different thicknesses. LS and NS denote longitudinal and normal stripes, respectively; f_{LN} is the crossover frequency separating the LS and NS states.
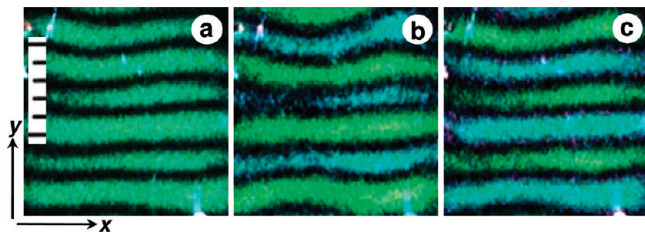
Patterned Electroconvective States

J. Phys. Chem. B, Vol. 114, No. 1, 2010 **13**

Figure 2. Longitudinal stripes observed along the easy axis *x* under white light illumination: (a) P(0)−A(90), (b) P(0)−A(100), and (c) P(0)−A(80); 10 kHz, 36.7 V (~$1.7V_c$); 10 μm scale division.

Figure 3. Two possible director configurations in the sample midplane corresponding to the LS texture. Nail heads indicate out of plane tilts. D and B represent dark and bright bands observed for crossed polarizers P(0)−A(90). (a) The out-of-plane θ and azimuthal φ director deviations increase or decrease together with the dark bands forming along *x* where the director is undisturbed. (b) θ and φ are out of step, with θ falling to 0 where φ is maximum and vice versa; the dark bands form along *x*, where the director is uniformly tilted in the *xz* plane.

in between. The dark stripes, if we suppose a trivial situation, form in the regions where the director is either undisturbed or tilted in the *xz* plane. As for the bright stripes, they appear alike in their birefringence colors. However, with marginally un-crossed polarizers, the adjacent bright bands display very different complementary colors, revealing the true periodicity to be double that in Figure 2a, which is ~3*d* at V_c. Comparison between Figure 2b for P(0)−A(100) and Figure 2c for P(0)−A(80) further shows the color interchange in adjacent bright bands for the two symmetrical positions of the analyzer axis relative to *y*. This fact, as also the very low light-focusing power of the periodic structure (see later), is indicative of a periodic azimuthal or inplane tilt $\varphi(y)$ as principally responsible for the colored bands in Figure 2. In other words, when light vibrating along $\mathbf{n_o}$ is incident, in the LS state, the nematic slab appears to transmit in general elliptic vibration with the ellipticity varying regularly as φ and being zero for $\varphi = 0$. However, this picture is simplistic for an important reason. Under planar boundary conditions, φ has to vanish at the substrates and is therefore expressible as $\varphi = \varphi_m \sin 2\pi y/\lambda \sin \pi z/d$, where φ_m is the midplane twist and λ the pattern periodicity. Propagation in the regions with structural helicity generally involves two eigenmodes which are elliptic vibrations with the major axes along and transverse to the local director. Under the adiabatic approximation of slowly varying twist or in the waveguide regime defined by the Mauguin parameter $u = \Delta nP/2\lambda = \Delta n\pi d/\Phi\lambda \gg 1$, with *P* as the pitch and Φ the total twist over distance *d*, the eigenmodes become linearly polarized along the electrical axes and follow the twist.[27a] Thus, for argument, if we were to take $d = 20$ μm, $\Delta n = 0.12$, and suppose a uniform twist with $\varphi_m = 20°$, the Mauguin condition would be very well satisfied ($u \approx 20$ for $\lambda = 0.55$ μm) and an incident vibration along or perpendicular to $\mathbf{n_o}$ would emerge without any change. In the absence of a sizable tilt or low Δn, we should therefore expect quenching of light for P(0)−A(90) even in the helical regions. Not only is this not observed, but light is generally not blocked in these regions for any of the orientations of P and A even in thick samples ($d \approx 50$ μm). The apparent breakdown of the Mauguin condition may be interpreted as follows. The true threshold pattern corresponding to low Φ and $u \gg 1$ does not reveal itself due to the waveguiding effect. The patterned state that becomes noticeable at first (Figure 2) indeed corresponds to a large enough value of Φ at which *u* is likely to be within 10.[27b] The out of plane tilt θ, when present, will also contribute to the lowering of *u* through reduced effective birefringence. Thus, V_c in Figure 1 is some value above the true threshold at which there is discernible transmission through the helical domains for P(0)−A(90). The gap between the true and optical thresholds reduces with lowering *d*. Here we may comment on whether the LS instability is a voltage or field effect. In Figure 1, we see $V_c(f)$ for the LS to be throughout higher for the thicker sample, but the increase is far from being proportionate to the thickness. It appears that the true threshold voltage is not
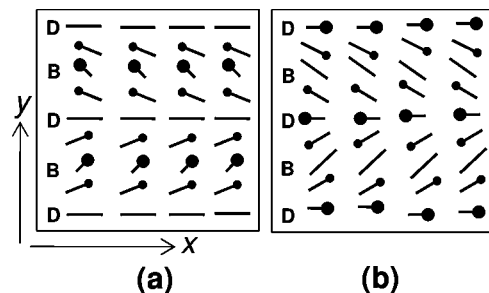
dependent on *d* and that the optical threshold increases only slightly with *d*.

On the basis of the foregoing optical observations, we may consider two possible field-induced director distributions in the sample midplane, as in Figure 3. In Figure 3a, the twist and tilt modulations are in phase, and in Figure 3b, the twist falls to zero where the tilt reaches its maximum and vice versa. Under P(0)−A(90), the dark (D) and bright (B) bands then form at the positions indicated in the figure. We examined the birefringence corresponding to the dark band regions at various *V* values using a Berek compensator, looking for evidence to choose between the two models. We found that in these regions $\Delta n(V)$ remained practically unvarying and equal to the birefringence of the unperturbed planar sample. Thus, between the two models, that in Figure 3b has to be excluded. However, there are other optical observations relating to the periodic wavefront modulation that do not directly follow from the model in Figure 3a as we shall presently discuss.

Light focusing by the nematic layer in the LS state is observable right at the optical threshold V_c, although it is generally inconspicuous and particularly weak at V_c. The following are the salient aspects of the lens effect not previously reported for any of the electroconvective patterned states. (a) Focusing of the incident parallel beam is observed with a single polarizer set either parallel or perpendicular to $\mathbf{n_o}$. For other orientations of P, the contrast diminishes with its minimum occurring for P(45) or P(135). (b) The real focal lines, for P(0), occur in the same positions as the bright bands of the interference pattern for P(0)−A(90). (c) In either the real R or virtual V image plane, the focal lines shift by ~$\lambda/2$ on changing the orientation of P or A from the ∥ to the ⊥ position relative to $\mathbf{n_o}$ (Figure 4a and 4b). (d) For P(0) or A(0), the V lines are sharper than the R lines (Figure 4c and 4d), and for P(90) or A(90) the reverse is the case. In general, the R and V planes are located asymmetrically with respect to the sample midplane (Figure 5). Thus, the outgoing corrugated wavefront exhibits an asymmetry determined by the initial polarization state. (e) The focal power for a given polarizer setting increases nonlinearly with voltage, tending to saturate in the high-voltage regime (Figure 5). (f) At higher voltages, a succession of real and virtual focal planes is discernible. Some of these results point to the inadequacy of simple director field models as in Figure 3. For instance, when using a single polarizer, since the extraordinary vibration experiences an index gradient transverse to $\mathbf{n_o}$ in either model, the light rays ought to acquire a curvature toward optically dense neighboring regions; thus, under P(0) for
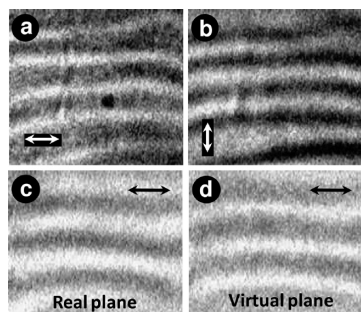
Figure 4. Focal lines in the LS state. Virtual lines shift by $\lambda/2$ with the incident electric vector changing from the (a) x to the (b) y direction. The real lines in c are more diffuse compared to the virtual lines in d; for P(90), the asymmetry in focal distances reverses. For P(45) or P (135), the illumination is practically uniform. The double-headed arrows show the polarizer direction; 28 V (= $1.04V_c$), 1 kHz, $T^* = 0.9580$.
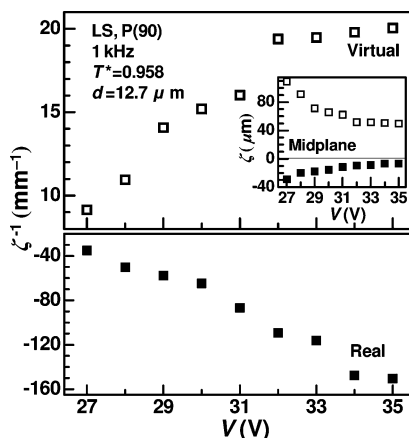

Figure 5. Focal power ζ^{-1} as a function of voltage, V, applied across the sample in the LS state; note the difference in ordinate scales for real and virtual images. (Inset) Voltage variation of focal length ζ (determined using the z-stacking facility of the microscope with the minimum step size of 0.01 μm). The optical threshold $V_c = 27$ V.
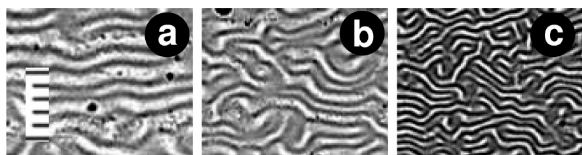

Figure 6. Textures demonstrating the voltage variation of periodicity in the LS state: (a) 70, (b) 90, and (c) 135 V. $f = 9$ kHz, $T^* = 0.9548$, $d = 13.4$ μm. Scale division = 10 μm.

argument, the real images are to be at positions D for the director pattern in Figure 3a but at B for that in Figure 3b. Experimentally, we observe the lines at B, but the model in Figure 3b does not conform to the $\Delta n(V)$ data for the D regions of Figure 3, as noted earlier. Furthermore, on changing the polarizer setting to P(90), the shift in the position of the images that occurs is difficult to explain in either model since the index field for the extraordinary vibration is not altered. Other possibilities such as field-induced biaxiality and dichroic absorption may have to be considered to fully account for the complex focusing effects.

The spatial period of conventional electroconvective rolls, for a sample of given d and at constant f, is known to be practically independent of the applied voltage.[28] On the other hand, LS show a remarkable decrease of wavelength λ_{LS} with increasing V. In Figure 6 demonstrating this effect, we also notice that the decrease in λ_{LS} comes about through an increase in the density of edge dislocations formed in the medium. Quantitatively, the wavenumber $\kappa = \lambda^{-1}$ of the stripes scales
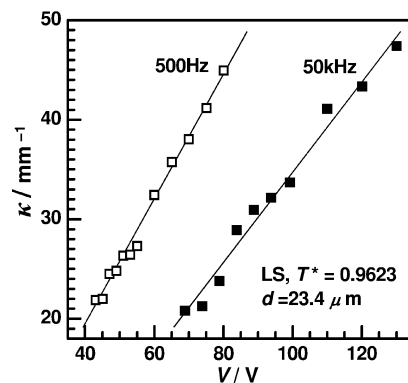

Figure 7. Wave number $\kappa = \lambda^{-1}$ of the longitudinal stripes pattern as a function of applied voltage for two field frequencies.
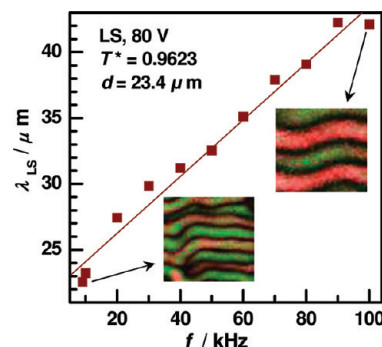

Figure 8. Frequency variation of the periodicity of LS. (Insets) Textures of LS observed at 10 kHz and 0.1 MHz.

linearly with V (Figure 7). Interestingly, very similar effects are also associated with the volume flexoelectric domains,[2] which are basically a static field phenomenon, rarely observed above ~10 Hz. The LS state, which occurs over a very wide band of frequencies, also exhibits a frequency-dependent periodicity; as shown in Figure 8, λ_{LS} increases linearly with f. Thus, an increase in f has the same effect as a decrease in V. This is of course a consequence of $V_c(f)$ (Figure 1) being an increasing function; this renders the distance from the threshold corresponding to a fixed bias to decrease with increasing f. In this context, we may clarify that in Figure 8 λ_{LS} is not the threshold period but the period corresponding to a fixed $V >$ V_c. In fact, the threshold period is practically f independent. For example, in a 23.4 μm thick sample, in the entire frequency region of occurrence of the LS, the period remained 52 ± 6 μm without any regular variational trend.

While $V_c(f)$ for the LS state at a given temperature is a generally increasing function, $V_c(T)$ at a given frequency increases monotonically only for lower frequencies below 10 kHz but shows a minimum for higher frequencies (Figure 9).

The LS instability is associated with a stationary, coordinated fluid flow. From the nature of drift of the dust particles suspended in the fluid, we find that the steady flow is coupled to the director field. The particles move parallel to x, along the lines along which the director is undisturbed, i.e., along the dark bands observed under P(0)−A(0). Further, the motion is opposite for adjacent flow lines. Thus, the vortices of flow, which are highly elongated along x, lie in the layer plane xy. Significantly, above the nematic−isotropic transition, no regular vortices of flow are indicated by the movement of dust particles.

Well above threshold ($V \approx 1.1V_c$) with the azimuthal and out-of-plane distortion amplitudes assuming large values, a new instability in the form of loop defects appears within the LS state. These defects possess the following regular features. (i)
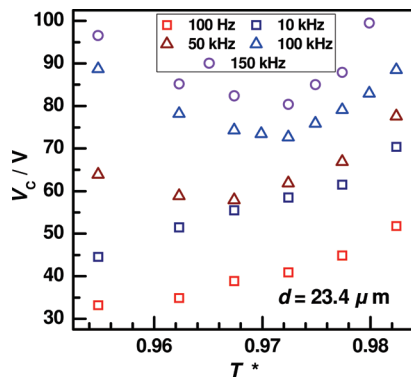
Patterned Electroconvective States

J. Phys. Chem. B, Vol. 114, No. 1, 2010 **15**

Figure 9. Temperature dependence of the optical threshold for the LS state at different field frequencies.

Figure 11. Crossover frequency between the threshold LS and NS states as a function of relative temperature.
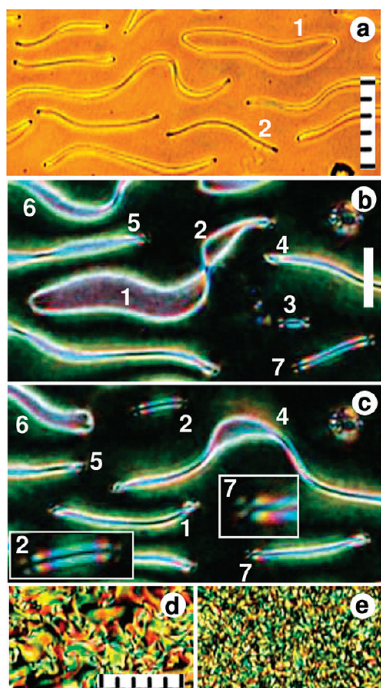

Figure 10. (a) Loop defects formed within the LS state in natural light. (b, c) Loop defects under P(0)−A(90); the images in b and c are of the same region, separated by a 30 s interval. Textures in (d) quasi-turbulent and (e) turbulent states, P(0)−A(90). $f = 1$ kHz. Voltages are (a−c) $1.15V_c$, (d) $1.8V_c$, and (e) $4.63V_c$. Scale: (a, d) 10 μm division; (b) 10 μm bar.

Figure 12. Near threshold textures of normal stripes under white light illumination showing changes in birefringence colors with orientation of crossed polarizers. Polarizer settings: (a) P(0), (b) P(15), (c) P(−15), (d) P(30), (e) P(−30), (f) P(45); 500 kHz, 22.4 V; $T^* = 0.9780$; $d = 12.7$ μm; $V_c = 19.8$ V; 10 μm scale division.

They originate in the regions of structural discontinuity like the cell boundaries and impurity sites. (ii) Viewed in natural light, they appear as relatively dark, narrow lines with bright bands on either side, as in loop 1 of Figure 10a. (iii) Under P(0)−A(90), the loop boundary is bright and the region enclosed by it shows birefringence color, as in loop 1 of Figure 10b; the light transmitted through the loop is not extinguished for any setting of the polarizers. (iv) The dynamics of the loops involves two unique features: First, the loops continually deform in a way as to end up as linear objects broadly parallel to the easy axis; such laterally collapsed loop disclinations (LCLDs), illustrated in Figure 10 (compare loops 1 and 2 in Figure 10b with their appearance in Figure 10c), sometimes also undergo the reverse effect. Second, the disclinations drift continually parallel to the easy axis, in some regions along $+x$ and in others along $−x$, and this propagation is correlated with the dust particle motion in these regions. Some of these properties are better appreciated in the video clip at (1) of the Supporting Informa-
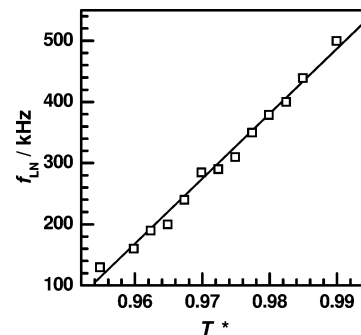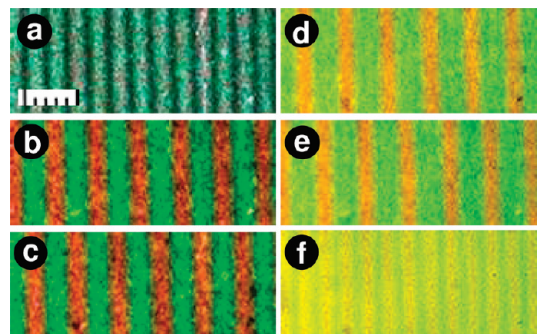
tion. At very high voltages, the loops become numerous and their motion increasingly random (Figure 10d and 10e).

Normal Stripes Instability. Now we turn to the normal stripes state which sets in at the primary bifurcation for frequencies beyond f_{LN} as shown in Figure 1. The NS pattern, with the effective wave vector $\mathbf{k}\|\mathbf{n}_o$, has previously been observed in three other bent-core systems and described as the prewavy texture.[18−21] For d and T held constant, with increasing $f > f_{LN}$, the optical threshold of the NS instability decreases sharply at first and then settles to a nearly constant value of a few volts. The wavevector crossover frequency f_{LN} is a linear function of temperature (Figure 11).

The NS, except for their orientation relative to $\mathbf{n}_o$, possess almost the same optical characteristics as the LS. We illustrate in Figure 12 the typical near-threshold appearance of the NS under white light illumination. The texture in Figure 12a for crossed polarizers P(0)−A(90), with the nematic director along x, shows periodic extinction of light along lines parallel to y with identical colored bands appearing in between. Under a slight rotation of the crossed polarizers with respect to (x, y), adjacent bright bands appear differently colored as in Figure 12b; for an equal rotation of the polarizers but in the opposite sense, the colors in adjacent bands interchange as in Figure 12c. These features once again indicate a periodic azimuthal modulation of the director, now along x, with the threshold wavelength of $\sim 3d$. When, under crossed polarizers, the angle β of the polarizer axis relative to $\mathbf{n}_o$ is gradually increased, the color separation between the adjacent bright bands progressively diminishes toward the diagonal $\beta = 45°$ position (Figure 12f). In analogy with the director patterns in Figure 3 for the LS, we may consider the possible distortion fields in Figure 13 for the NS. Here too the finer aspects of light focusing, which are the same as listed for the LS, demonstrate the inadequacy of
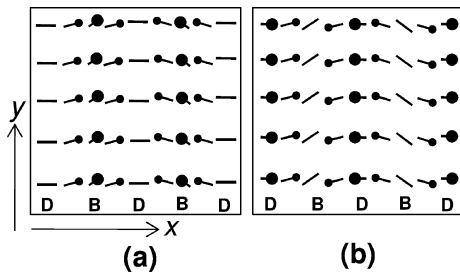
Figure 13. Two possible director configurations in the sample midplane corresponding to the NS texture. Nail heads indicate out of plane tilts. D and B represent dark and bright bands observed for crossed polarizers P(0)−A(90). (a) The out-of-plane θ and azimuthal φ director deviations increase or decrease together with the dark bands forming along y, where the director is undisturbed. (b) θ and φ are out of step, with θ falling to 0 where φ is maximum and vice versa; the dark bands form along y, where the director is uniformly tilted in the xz plane.
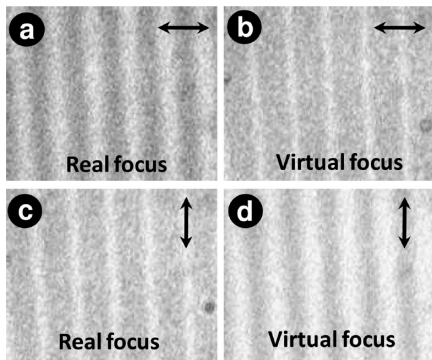

Figure 14. NS texture observed at $T^* = 0.9580$ with a single polarizer showing contrast reversal on changing the polarizer orientation between P(0) and P(90) in either the real or the virtual focal plane. Double-headed arrow indicates the polarizer setting. $V = 1.55V_c, f = 300$ kHz. Focusing of light becomes noticeable in the NS state well above V_c, whereas in the LS state it is discernible even slightly above the threshold.

these simple models. For instance, in Figure 14 we show the line images in the real and virtual planes recorded using a single polarizer. The real images for P(0) are again located at the bright fringe positions of the interference pattern for P(0)−A(90), supporting the model in Figure 13b; however, $\Delta n(V)$ for the dark fringe regions D does not provide any evidence of director tilt in these regions. Also, the effective shift of the images by $\lambda/2$ in going from P(0) to P(90) in either focal plane is not anticipated from the index fields in either model.

In the NS state, as in the LS state, a succession of focal planes is observed (Figure 15). With P(0), the focal power is more for the virtual images than for the real ones, and with P(90) the converse is observed. Figure 16 illustrates this difference in focal powers quantitatively. Corrugation of the extraordinary wave-front during passage through a nematic layer is basically a result of periodic out of plane tilt modulations. It is interesting to recall here the focusing by the lattice of cylindrical lenses formed in the conventional Williams domain mode (WDM) of electro-convection. There it is shown[28,29] that the focal power is given by $\zeta^{-1} = \Delta n\theta_o^2 q^2 d$, where θ_o is the maximum midlayer tilt decaying harmonically toward the substrates and the wavenum-ber $q \approx \pi/d$. For V not far above V_c, the maximum tilt is given by $\theta_o^2 = A[(V/V_c) − 1]$ with A involving various electrical and hydrodynamic parameters. Thus, ζ^{-1} is expected to be linear in V initially; as θ_o saturates for $V \gg V_c$, the focal power is expected to rise to a steady value in the far field regime. The $\zeta^{-1}(V)$ plot in Figure 16 largely conforms to these predictions
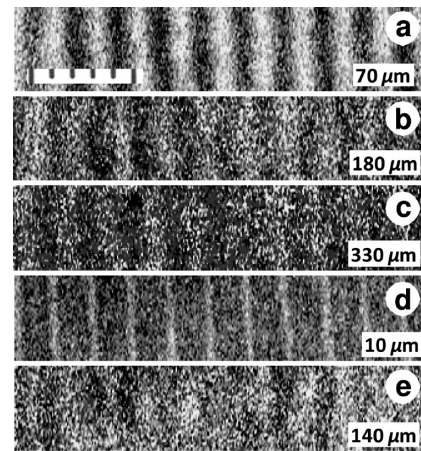

Figure 15. Succession of focal planes observed with P(0) in the NS state at $T^* = 0.9580$: (a−c) real planes and (d,e) virtual planes. The distances given are the focal lengths. $f = 500$ kHz; $V = 1.9V_c$; $d = 12.7$ μm; 10 μm scale division.
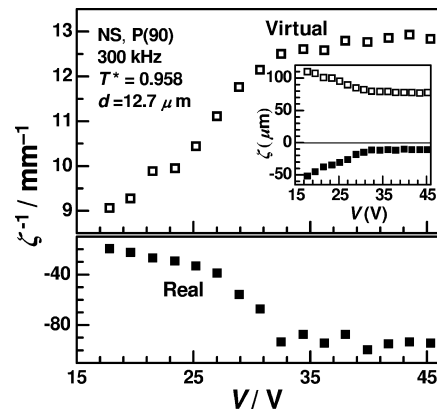

Figure 16. Focal power ζ^{-1} as a function of voltage V applied across the sample in the NS state; note the difference in ordinate scales for real and virtual images. (Inset) Voltage variation of focal length ζ (determined using the z-stacking facility of the microscope with the minimum step size of 0.01 μm). The optical threshold $V_c = 15$ V.
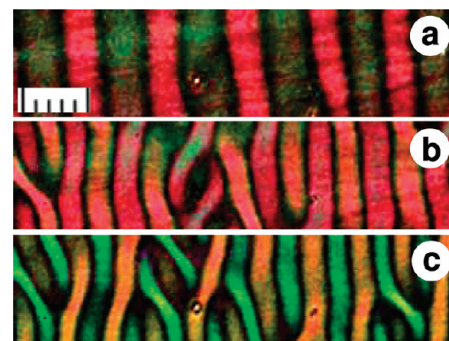
Figure 17. Textures demonstrating the voltage variation of periodicity in the NS state under P(0)−A(75): (a) 15, (b) 25, and (c) 35 V; $f = 0.8$ MHz; $T^* = 0.9580$; $d = 13.4$ μm. Scale division = 10 μm.

for the WDM, although the initial increase in ζ^{-1} is not quite linear. The trends in Figure 5 for the LS are also similar.

Just as the LS, NS show a general decrease of their spatial period λ_{NS} with increasing V. In Figure 17, demonstrating this effect, we also notice that the decrease in λ_{NS} comes about through an increase in the density of edge dislocations formed in the medium. Quantitatively, the wavenumber κ of the stripes scales nearly linearly with V except close to V_c where the variation is not significant (Figure 18). Further, the dependence of κ on V is remarkable only in the high-frequency region; unlike

Patterned Electroconvective States

J. Phys. Chem. B, Vol. 114, No. 1, 2010 **17**

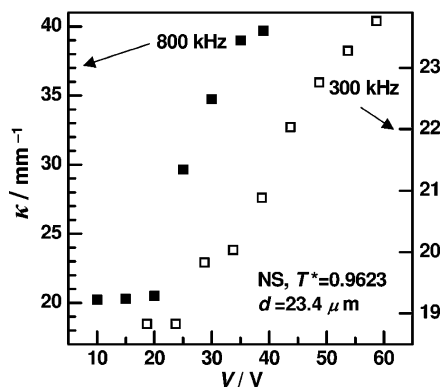**Figure 18.** Wave number $\kappa = \lambda^{-1}$ of the normal stripes pattern as a function of applied voltage for two field frequencies.
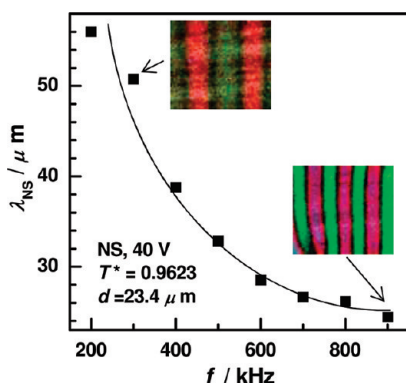

Figure 19. Frequency variation of the periodicity of NS. (Insets) Textures of NS observed at 0.3 and 0.9 MHz.

Figure 20. Optical threshold of the NS instability as a function of the relative temperature at a fixed frequency.

for LS, κ varies very little when f is low, as evident from the plot for $f = 300$ kHz in Figure 18. The NS state, which occurs over a very wide band of frequencies, also exhibits a frequency-dependent periodicity. It is significant that, opposite to the trend seen in Figure 18 for the LS, λ_{NS} decreases with increasing f at a given bias (Figure 19). Thus, an increase in f has the same effect here as an increase in V. This is of course a consequence of $V_c(f)$ (Figure 1) being a decreasing function; this renders the distance from the threshold corresponding to a fixed bias to increase with f. Here, we may clarify that in Figure 19 λ_{NS} is not the threshold period but the period for a fixed $V > V_c$. In fact, the threshold period is practically f independent as for the LS. For example, in a 23.4 μm thick sample, the period remained 57 ± 6 μm in a broad band of frequencies and the variations had no regular trend.

In the NS state, $V_c(T)$ at a fixed frequency increases monotonically as in Figure 20.

The NS instability, again like the LS instability, is associated with a stationary flow field, and the streamlines are confined to the layer plane xy (see Figure 1, pdf file (3), Supporting Information); we observed in a 12.7 μm thick sample, at $V = 2.7V_c$, tiny dust particles to drift along $\pm y$ with a speed of ~ 1 μm s^{-1}. No coordinated flows exist above the nematic−isotropic temperature.

In the high-voltage regime, the secondary instabilities arising within the NS state are yet again as in the LS state. The LCLDs, which stretch now in a direction transverse to $\mathbf{n}_o$, often originate at one of the sample edges normal to the streamlines and decay at the other opposite edge. Impurity sites also act as sources and sinks for the loop defects. These defects drift continually in the flow direction. Quite frequently, defects having a common drift direction, either y or $-y$, tend to form colonies; in other
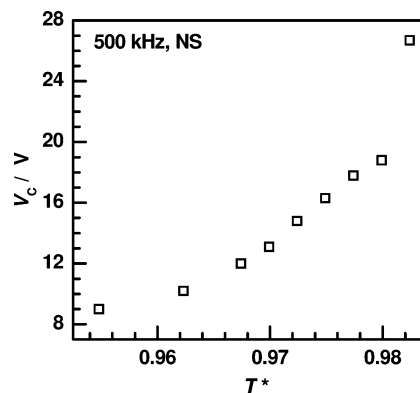
words, the spatial separation between the defect columns is usually the domain period. In Figure 21a exemplifying this feature, the polarizer setting is P(0)−A(90); the LCLDs are along alternate flow lines and the extinction bands between them are free of any thread defects. Oppositely moving loops are usually well separated along x, as illustrated in Figure 21a and 21c. When a drifting LCLD encounters an edge dislocation of negative sign, its progress is arrested and it shrinks in length to eventually disappear, as in Figure 21d and 21e; on the other hand, when it arrives at a positive dislocation, it continues to drift along either of the bifurcated streamlines matching with the drift direction, as in Figure 21f and 21g. Some of these aspects are better appreciated in the video clip at (2) of the Supporting Information.

At very high fields, the loop defects become irregular in shape and the patterned state on the whole becomes time dependent (Figure 21h).

3.2. Comparative Discussion of the Instabilities: Parallel vs Longitudinal Stripes. We may compare our results for **CNRbis12OBB** with those for compounds **1**, **3**, and **nCN**.[17,18,21] Let us consider first the parallel stripes PS in compound **1**.[18] Although these are oriented along the easy axis $\mathbf{n}_o$ and are readily observed through interference of polarized light just as the LS, the two textures correspond to very different electroconvective states. (a) PS occur only in the $(- -)$ regime, over a narrow frequency range (1−28 Hz), but LS form over a very vast frequency window covering both $(- -)$ and $(- +)$ regimes. (b) The period of PS is less than d, whereas that of LS is between $2d$ and $3d$. (c) The observed threshold voltage of the PS state is linear in f, but that of the LS state comprises three different largely linear parts. (d) At a fixed f, $V_c(T)$ decreases linearly for PS, but for LS it is generally nonlinear, being an increasing function in the low-frequency $(- -)$ region and having a minimum at higher frequencies. (e) PS are localized, while LS are extended. We may mention here that for static and very low f (<15 Hz) fields, instead of a regular modulation as in PS, a variety of unspecific threshold patterns develop in **CNRbis12OBB** that become strongly time dependent at higher voltages. It is relevant to recall here the static field-induced instabilities reported by Kovalenko et al.[17] for thin samples ($d = 6$ μm) of **8CN**. As earlier mentioned, they observe stripes with $\mathbf{k} \perp \mathbf{n}_o$ and a threshold period ~ 1.67 d ($d = 6$ μm) that reduces to ~ 1.33 d at twice the threshold. As the voltage increases further, the scenario alters drastically: the pattern changes into a myeline texture with very fine stripes, and this is followed by a transformation into a smectic-like fan texture that is free of stripes. Obviously, this sequence of events differs from the one observed here for thick samples under ac driving,
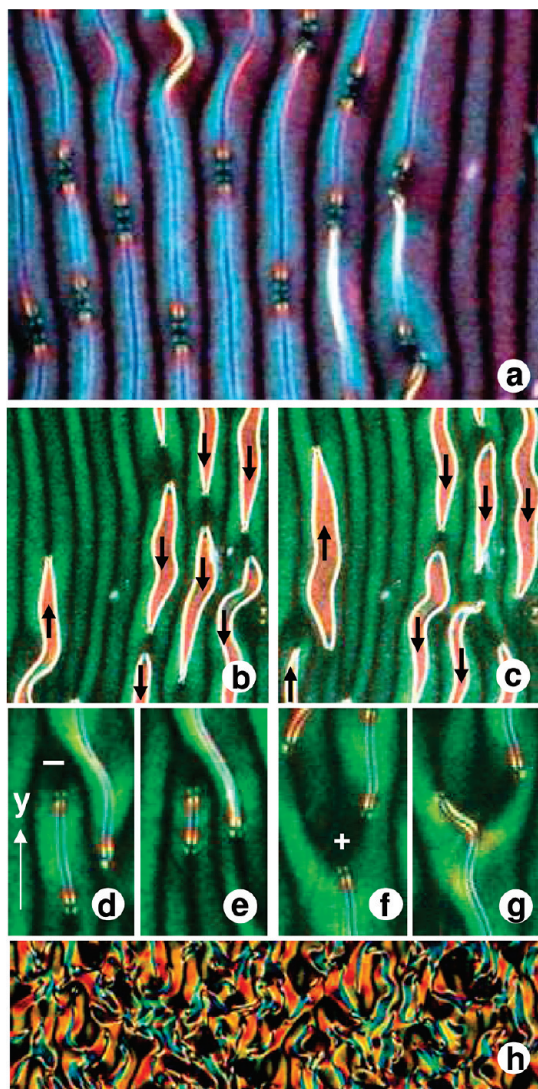
Figure 21. Loop defects formed in the NS state in a sample of 12.7 μm thickness, observed under P(0)−A(90), at $T^* = 0.9580$. (a) Laterally collapsed loop defects (LCLDs) lined up end to end along downward streamlines and drifting continually downward; the dark bands alternating with the defect chains are along upward streamlines; $f = 0.5$ MHz, $V = 5.4V_c$. (b, c) Images of oppositely drifting loop defects captured at an interval of 15 s; the arrows indicate the drift directions; $f = 0.5$ MHz, $V = 3.4V_c$. (d, e) Images of a LCLD at an interval of a few seconds, demonstrating the decay of the defect at a negative edge dislocation. (f, g) Images of a LCLD at an interval of a few seconds, demonstrating the passage of the defect along a bifurcation branch at a positive edge dislocation; $f = 0.5$ MHz, $V = 3.4V_c$. (h) Quasi-turbulent state into which the NS instability passes at very high fields; $f = 0.3$ MHz, $V = 6.0V_c$.

indicating the sensitivity of the electrical response to both d and f. Stripes with $\mathbf{k} \perp \mathbf{n}_o$ are also observed in the uniaxial nematic phase of compound **3** and described as the PW1 texture despite the periodicity of the pattern being $\sim d$. The wavevector direction of this PW1 mode is attributed to the twist elastic modulus being an order of magnitude lower than the splay and bend moduli; this is said to favor a periodic twist-modulated structure at lower fields. By contrast, the structure of LS involves both inplane and out of plane modulations.

Director Modulations with $\mathbf{k} \perp \mathbf{n}_o$. Observation of electroconvective rolls parallel to the preferred alignment direction has a long history associated with calamitic systems belonging to the $(-- \mathrm{p})$ class.[9,11,30−33] While in all these studies the pattern period shows a uniform trend ($\lambda < 1.5d$), the nature of

modulations seems to vary between two types. Thus, in some cases, the director deviations are confined to the $\mathbf{E}-\mathbf{n}_o$ plane, rendering the patterns visible through shadographic imagery,[30,31] while in others they occur primarily in the layer plane, so that birefringence contrast is found to be the best means of visualizing the corresponding patterns.[9,11] The instability is interpreted variously as due to the modified CH mechanism under twist fluctuations[30] or pretilt coditions,[32] an isotropic electrolytic mechanism involving charge density gradients along the field,[9,31] and the coupling between CH and flexoelectric mechanisms.[13,14,35,36] For the $(-- \mathrm{p})$ case, it follows from eq 1 that the SM instability is excluded.[15−18] Interestingly, however, as shown by Madhusudana and Raghunathan,[34a] when flexoelectric terms are incorporated into the one-dimensional CH theory for the $(-- \mathrm{p})$ case, electroconvection becomes possible. Significantly, the theoretical-numerical analysis in ref 34a for certain chosen values of material parameters, while providing no solution corresponding to the conduction regime, shows the existence of a nearly longitudinal roll instability in the dielectric regime characterized by the field threshold. Recent analyses that extend the SM by inclusion of the flexoterms,[13,14] while reconfirming the predictions in ref 34a, point to the importance of flexoeffects particularly in thin cells and for low frequencies. These theoretical advances do not seem to address two important aspects associated with the LS instability: First, its observation in thick samples at very high frequencies which severely reduces the influence of flexoelectricity; and second, its occurrence involving the director modulations predominantly in the layer plane with a large periodicity.

The LS instability is more like the PW2 instability observed in **1** and **2**, although the wavevectors for the two states differ, being in orthogonal directions. For example, the period λ relative to d and the rising $V_c(f)$ trend are similar in both cases, and both instabilities undergo transition into the time-dependent state through defect mediation. However, the two states differ in one significant aspect. The LS state extends well into the $(- +)$ region, but the PW2 is confined only to the $(- -)$ region. This might just indicate that anisotropic σ is not a decisive factor for the formation of either the LS or the PW2 instability. Nevertheless, it does play a part as evidenced by a discontinuous change in the slope of the $V_c(f)$ curve at the conductivity isotropy point f_1 (see Figure 5, ref 26).

Very High Frequency Instabilities. Coming to the NS pattern, it is qualitatively very similar to the PW1 texture in compounds **1** and **2** as far as $V_c−f$ and $\lambda−V$ variations are concerned. However, the PW1 mode occurs in both $(- +)$ and $(- -)$ regions of compound **1**, whereas the NS mode is found exclusively in the $(- -)$ region. Further, under steady conditions, λ is practically independent of f in compound **1**, but λ is a strongly decreasing function of f in **CNRbis12OBB**.

An important feature in the phase diagram of compound **1** is the existence of a stability zone (ER) between the PW2 and the PW1 regimes for which $V_c{}^{-1}(f)$ is found to be linear with the extrapolated lines showing a f gap even at $V_c{}^{-1} = 0$. On the other hand, for compound **2**, a brief mention is made of the existence of a region of obscure PW pattern between the PW2 and PW1 regions.[19] In **CNRbis12OBB**, as could be deduced from Figure 1, $V_c{}^{-1}(f)$ is nonlinear for both LS and NS instabilities and there is no intervening gap between the two states; in fact, in a narrow region above f_{LN}, the threshold NS pattern disappears at higher voltages and, with further increase in V, the LS pattern re-emerges. This may well be due to sample heating, which may be considerable for large V and f; it could take the sample into the regime below f_{LN}.

Patterned Electroconvective States

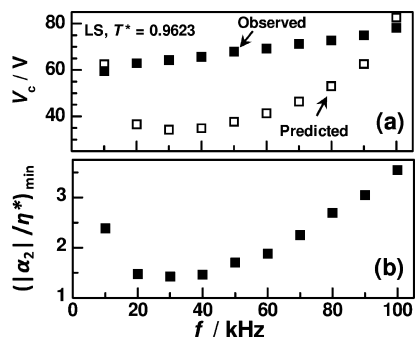*J. Phys. Chem. B, Vol. 114, No. 1, 2010* **19**

Figure 22. (a) Comparison of the threshold voltage given by eq 2 with the observed threshold for the $(- +)$ region of the LS instability. (b) Minimum value of the ratio of viscosity coefficients, $|\alpha_2|/\eta^*$, imposed by eq 1 for the appearance of the instability in the $(- +)$ region.

Regarding the flow field, Wiant et al.[18] describe the most frequently observed dust particle trajectory in compound **1** as zigzag lines along the director. The particle speeds are stated as rather low, requiring several hours to cover 0.5 mm. They also mention particle motion in opposite directions transverse to $\mathbf{n}_o$. In **CNRbis12OBB**, as mentioned earlier, suspended particles move along the stripes with relatively much greater speeds of $\sim 1\ \mu$m/s. The flow direction appears to have its origin in the director tilt having both θ and φ components. This would imply the existence of current densities along both x and y, transverse to the applied field.

Large Period Normal Stripes Texture. Domains having a periodicity around $3d$ and $\mathbf{k}||\mathbf{n}_o$ were observed early in calamitic systems.[35–38] Trufanov et al.,[37] who studied this instability in 4-methoxybenzylidene-4′-butylaniline (MBBA) and other similar $(- +)$ compounds, described it as the broad domain (BD) mode arising under high-frequency excitation in high-conductivity nematics. Significantly, the BDs appearing normal to $\mathbf{n}_o$, unlike the NS, were exclusively due to periodic inplane modulations, not involving any out of plane deviations. They were regarded as an anisotropic effect and analyzed through an adaptation of the CH mechanism, taking into account the inertial effects.[38] The expression for the threshold thereby obtained is

$$V_c = 2\pi\omega[\varepsilon_o\varepsilon_m k_m/(\sigma_m\sigma_a)]^{1/2} \qquad (2)$$

where ε_m, k_m, and σ_m are the mean values of dielectric, elastic, and conductivity constants. Evidently, this equation rules out the instability for $\sigma_a < 0$. The NS state corresponding to the $(- -)$ situation is thus not explained by the theory. The result of applying eq 2 to the LS state in the $(- +)$ regime is shown in Figure 22a. It is to be noted that the actual threshold is likely to be smaller than the optical threshold. Despite the order of magnitude agreement between the observed and predicted thresholds, the extended CH model deviates from the experimental findings in two important respects. First, it considers the wave vector along $\mathbf{n}_o$; second, the symmetry of the linear mode according to the model corresponds to modulations of the director in the vertical xz plane rather than the layer plane xy. It has been argued[38] that this latter deviation might be due to some initial pretilt at the substrates or nonlinear velocity and director deviations. However, other mechanisms like the dynamic flexoelectric effect[39] that affects the relaxation of azimuthal modulations[40] might need to be considered.

An important feature of the stripes in **CNRbis12OBB** is that their critical periodicity is independent of frequency. This may appear surprising when we recall that, in conventional EC, the critical wavenumber q_c is an increasing function of f. However,

when flexoelectric parameters are incorporated into the standard model description of EC, $q_c(f)$ varies differently for different σ_a values and becomes flat for negative σ_a.[13] More significantly, in the extended CH model incorporating the inertial effects,[2] q_c turns out to be independent of f. Experimentally, this situation is obtained for the wide domains considered to belong to the inertia mode.[37] Indeed, the LS and NS instabilities have much in common with the BD mode including the inlayer vortices coupled to the director field and constancy of q_c with respect to f.

Apart from the BD mode, there exists another large-period mode with $\lambda \approx 4d$-$6d$, which has been described as the prewavy instability since it happens to transform spontaneously into a propagating sinusoidal pattern.[41] These stripes form in initially homeotropic $(- +)$ calamitics, in the quasiplanar base state, far above the bend Freedericksz transition, with the wavevector transverse to the tilt plane. This instability continues into the isotropic phase, and its periodicity is unaffected by V and f. Evidently, the instabilities in **CNRbis12OBB** are to be distinguished from the PW mode, the origin of which involves the electrolytic isotropic mechanism.

Nonstandard Instabilities in the Dynamic Regime of Electrical Parameters. Is the SM instability expected to occur in **CNRbis12OBB** at least in the frequency region corresponding to the $(- +)$ situation? From eq 1 it is readily seen that to have a real threshold the following condition needs to be met

$$\varepsilon_o\varepsilon_a^* - \frac{\alpha_2\tau_q\sigma_a}{\eta^*} > 0 \qquad (3)$$

This imposes a limit on the minimum value of the viscosity ratio $|\alpha_2|/\eta^*$; we calculated this value, $(|\alpha_2|/\eta^*)_{min}$, for $T^* = 0.9623$ making use of the physical constants in ref 26.[42] As seen in Figure 22b, for various frequencies in the range 10–100 kHz, $(|\alpha_2|/\eta^*)_{min}$ lies between 1.4 and 3.6. For calamitics, $|\alpha_2|/\eta^*$ is usually less than 1.[5] For the BC nematic **ClPbis10BB**, recent measurements indicate that while the rotational viscosity is some 10 times larger than for calamitics, the flow viscosities are larger by two orders (see ref 26 and references therein). Since the rotational viscosity may be taken nearly equal to $|\alpha_2|$, the ratio $|\alpha_2|/\eta^*$ is likely to be considerably lower than the required minimum for pattern formation by the CH mechanism. Understandably, the patterns in BC nematics do not conform to the SM. There is however a serious limitation to eq 1 when dealing in the dynamic regime of the electrical parameters ε and σ. In almost all the numerical studies on anisotropic electroconvection where the SM has been applied, the frequency regime considered does not involve relaxation of ε and σ (see, e.g., refs 5, 13, and 14). In the neighborhood of dielectric dispersion, the electrohydrodynamic scenario involves $\varepsilon''\omega$, which acts as a charge source term. Anisotropy of dielectric loss $(\varepsilon_{||}'' - \varepsilon_{\perp}'')$ then generates space charges that could couple to a splay-bend curvature.[43a–c] Since the usual expression of charge relaxation frequency does not apply to these space charges, electroconvective effects are anticipated[43c–f] in the high-frequency dynamic domain. Such effects have also been observed in both calamitic[43a,b,e,f] and BC systems.[22,23] Figures 2 and 3 of ref 26 clearly show that beyond 10 kHz we cannot ignore the effects of relaxation in **CNRbis12OBB**. This situation is perhaps common to many BC nematics, and thus, any theory developed to account for the anisotropic convection in these liquid crystals cannot ignore the complex electrical parameters.

Director Distribution in the Patterned States. An important feature of the patterned states in BC nematics to which attention is drawn in ref 19 is the nonextinction of light in the deformed

stripe regions for any of the settings of polarizer and analyzer. As earlier mentioned, this is taken to imply a chiral order in these regions with the twists in adjacent distorted zones being of opposite sense; correspondingly, the planar anchoring at the substrates is thought to acquire a periodic inplane twist and become degenerate. While this is a possibility, the director configurations provided in Figures 3 and 13 do not seem to disagree with the transmission of light under all possible P−A orientations. The Mauguin waveguide effect is achromatic only when the optical path corresponding to the effective pitch is very large compared to the wavelength. Otherwise, the dispersion of birefringence would render the transmission wavelength dependent, so that in white light total light extinction may not be possible for any P−A combination.

Periodic Disclination State. The disclination loops and LCLDs are complex structures arising under high fields. The loops could indeed be visualized as twist disclinations formed when the amplitude of azimuthal modulation becomes so large that the unperturbed regions, to reduce energy, acquire a π twist across the sample thickness with the director in the midplane switching over from the x to the y direction. Additional θ distortion would explain the interference colors within the loops. We may recall here that in planar samples 1/2 strength loop threads are known to form between undistorted and π-twisted regions.[44] The texture of these threads resembles that in Figure 21. Also, the width of the defect lines (~ 2 μm) in our case is of the usual order for the 1/2 strength twist lines. Regarding the disclination dynamics, irregularly shaped twist loops are generally metastable, assuming a circular steady form as they collapse, and this is in accord with the theoretical prediction based on the assumption of elastic isotropy.[44] Instead, in the present case, presumably due to a large elastic anisotropy, the collapse is principally in the direction transverse to $\mathbf{n}_o$. Further, the LCLDs, as seen in inset 2 of Figure 10c, do not always shrink and disappear. Their complex behavior includes lengthwise decay and growth, wavy deformation, division, association, and continual coordinated propagation. The birefringence colors that the LCLD displays are typical. A median dark line divides it laterally; it often terminates in Maltese crosses that may deform into hyperbolic brushes during its complex dynamics. As a rule, the polarization colors decrease from the midregion of the LCLD toward the center of the Maltese crosses, indicating a corresponding increase in the director tilt. From these optical features it appears that the 1/2 strength loops collapse laterally into a +1 defect line with the end regions remaining semicircular. Thus, the defect as a whole is topologically equivalent to a hedgehog.

The loop disclinations may form differently for reasons of θ distortion becoming large. Then 'pincement'[45] may set in to generate a pair of 1/2 strength disclinations along y; these lines lie in the yz plane through the originally unperturbed region, the director between them having switched from the x to the z direction in pincement. They get connected end to end via twist deformations to form a loop confined to the yz plane. The topological equivalence of wedge and twist defects of either sign is evident in the formation of such loops.

The LCLD instability is, in some ways, reminiscent of the CRAZY (convection in a regular array of $z−y$ disclination loops) roll state in a conventional (− +) nematic with homeotropic anchoring.[46] The CRAZY state follows the bifurcation sequence: Bend-Freedericksz → NRs → ARs (abnormal rolls). Each CRAZY roll is thought to contain two singular lines attached to the surfaces and running parallel to the roll axis in the yz plane. These lines join at the ends to form a loop. For both the LCLD and CRAZY structures, the broken $y \rightarrow −y$ symmetry could lead to propagation along the stripes. However, no motion is reported for the disclinations of the CRAZY rolls; in fact, these disclinations seem unstructured along y. Thus, any velocity component along y they might possess would be difficult to perceive. On the other hand, LCLDs terminate in extinction crosses and are clearly separated along y from one another, so that their dynamics is readily noticed. More fundamentally, the dynamics of LCLD is related to the inplane vertical flows not having a parallel in conventional electroconvection.

Route to the Turbulent State in Straight and Bent-Core Nematics. In rod-like (− +) nematics, the sequence of EC structures occurring beyond the Lifshitz point is as follows: normal rolls (NRs)-undulatory normal rolls (UNRs)-oblique rolls (ORs)-skewed varicose (SV)-2D or bimodal (BM)-dynamic scattering mode 1 (DSM1) and DSM2.[8] Usually, at the stage of bifurcation into the OR state, edge dislocations appear as a means of adjustment to the varying wave vector field. Oscillatory ORs occur in the process of formation of 2D structures due to the high mobility and density of defects. DSM1 is observed when the grid patterns repetitively break up to form short oblique rolls and reform; then, closed singular loops form within each of the rolls. At higher fields, nucleation of tiny, nearly circular loop disclinations that travel at high speeds within the fluid leads to DSM2.[47,48]

The route to chaos in **CNRbis12OBB** differs from the above scenario for the standard EC. This is understandable since the stripes in the BC nematic are essentially of nonstandard origin and cannot be explained by the CH mechanism. Yet, the turbulent state here is arrived at through the intermedium of loop disclinations subsequent to the formation of edge dislocations, just as in (− +) calamitics. However, these singular defects are highly ordered with regard to their spatiotemporal behavior unlike in calamitics. They are also unstable against fluctuations transverse to their length and tend to render the stripe domains with which they are associated undulatory. In fact, even prior to their formation and particularly at low frequencies, the LS and NS structures seem to turn increasingly wavy as the field is elevated (see Figures 2 and 3, pdf file (3), Supporting Information). However, the wavelength here decreases (Figure 6) with an increase in control parameter, unlike for the UNRs.

Conclusions

The study reveals that in the nematic **CNRbis12OBB** the threshold instabilities manifest optically as periodic stripes with the wave vector either transverse to the easy axis (LS) or parallel to it (NS). This is the first observation of the occurrence of the LS state over a very broad frequency band in a BC system. The study reveals some interesting qualitative and quantitative details pertaining to the polarization-dependent light focusing by the deformed fluid. It also points to the order that exists with regard to the structure and dynamics of twist disclinations that occur on the route to turbulence.

But for their opposite $V_c(f)$ trends and differing $\mathbf{k}$ directions, the two states are very similar in their other characteristics relating to director modulation, light focusing, wavenumber dependence on V, and secondary instabilities leading to turbulent flows. These anisotropic instabilities are inexplicable on the basis of either the SM or the extended CH theory incorporating the inertial term. In view of the dielectric and conductivity relaxation effects falling well within the frequency regimes wherein these instabilities are exhibited, it is necessary to consider the space charge contribution due to the anisotropic dielectric loss in any

Patterned Electroconvective States

J. Phys. Chem. B, Vol. 114, No. 1, 2010 **21**

analysis of the problem. It is also important to note that the optical threshold in thick samples is likely to be an overestimate of the true threshold because of the Mauguin condition.

Supporting Information Available: (1) A video clip showing coordinated unidirectional drift of disclination arrays in the longitudinal stripes state of nematic **CNRbis12OBB**, observed using polychromatic light, crossed polarizers with their axes along the vertical (y) and horizontal (x) picture-edges, initial alignment along x, $V = 39$ V $= 1.3$ V$_c$, $f = 10$ kHz and $T^* = 0.9623$. (2) A video clip of unidirectionally traveling disclination arrays in the normal stripes state for $V = 54$ V $= 4.9$ V$_c$, $f = 500$ kHz and other conditions as in (1). (3) A pdf file providing the details of flow field (Figure 1) and secondary undulatory instability in the stripe-states (Figure 2). This information is available free of charge via the Internet at http://pubs.acs.org.

References and Notes

(1) Blinov, L. M.; Chigrinov, V. G. *Electrooptic Effects in Liquid Crystal Materials*; Springer: Berlin, 1994.

(2) Pikin, S. A. *Structural Transformations in Liquid Crystals*; Gordon and Breach Science Publishers: New York, 1991.

(3) Helfrich, W. *J. Chem. Phys.* **1969**, *51*, 4092.

(4) Dubois-Violette, E.; de Gennes, P. G.; Parodi, J. *J. Phys. (Paris)* **1971**, *32*, 305.

(5) Bodenschatz, E.; Zimmermann, W.; Kramer, L. *J. Phys. (Paris)* **1988**, *49*, 1875.

(6) Kramer, L.; Pesch, W. In *Pattern Formation in Liquid Crystals*; Buka, A., Kramer, L., Eds.; Springer: Berlin, 1996.

(7) Scheuring, M.; Kramer, L.; Peinke, J. *Phys. Rev. E* **1998**, *58*, 2018.

(8) Ribotta, R. In *Solitons in Liquid Crystals*; Lam, L., Prost, J., Eds.; Springer: Berlin, 1992.

(9) Kochowska, E.; Nemeth, S.; Pelzl, G.; Buka, A. *Phys. Rev. E* **2004**, *70*, 011711.

(10) (a) Buka, A.; Eber, N.; Pesch, W.; Kramer, L. In *Self Assembly, Pattern Formation and Growth Phenomenon in Nano-Systems*; Golovin, A. A.; Nepomnyashchy, A. A., Eds.; Springer: Berlin, 2006. (b) Buka, A.; Eber, N.; Pesch, W.; Kramer, L. *Phys. Rep.* **2007**, *448*, 115.

(11) Toth-Katona, T.; Cauquil-Vergnes, A.; Eber, N.; Buka, A. *Phys. Rev. E* **2007**, *75*, 066210.

(12) Kumar, P.; Patil, S. N.; Hiremath, U. S.; Krishnamurthy, K. S. *J. Phys. Chem. B* **2007**, *111*, 8792.

(13) Krekhov, A.; Pesch, W.; Eber, N.; Toth-Katona, T.; Buka, A. *Phys. Rev. E* **2008**, *77*, 021705.

(14) (a) Toth-Katona, T.; Eber, N.; Buka, A.; Krekhov, A. *Phys. Rev. E* **2008**, *78*, 036306. (b) May, M.; Schopf, W.; Rehberg, I.; Krekhov, A.; Buka, A. *Phys. Rev. E* **2008**, *78*, 046215.

(15) Pelzl, G.; Eremin, A.; Diele, S.; Kresse, H.; Weissflog, W. *J. Mater. Chem.* **2002**, *12*, 2591.

(16) Weissflog, W.; Sokolowski, S.; Dehne, H.; Das, B.; Grande, S.; Schroder, M. W.; Eremin, A.; Diele, S.; Pelzl, G.; Kresse, H. *Liq. Cryst.* **2004**, *31*, 923.

(17) Kovalenko, L.; Schroder, M. W.; Reddy, R. A.; Diele, S.; Pelzl, G.; Weissflog, W. *Liq. Cryst.* **2005**, *32*, 857.

(18) Wiant, D.; Gleeson, J. T.; Eber, N.; Fodor-Csorba, K.; Jakli, A.; Toth-Katona, T. *Phys. Rev. E* **2005**, *72*, 041712.

(19) Tanaka, S.; Dhara, S.; Sadashiva, B. K.; Shimbo, Y.; Takanishi, Y.; Araoka, F.; Ishikawa, K.; Takezoe, H. *Phys. Rev. E* **2008**, *77*, 041708.

(20) Tanaka, S.; Takezoe, H.; Eber, N.; Fodor-Csorba, K.; Vajda, A.; Buka, A. *Phys. Rev. E* **2009**, *80*, 021702.

(21) Xiang, Y.; Goodby, J. W.; Gortz, V.; Gleeson, H. F. *Appl. Phys. Lett.* **2009**, *94*, 193507.

(22) Kumar, P.; Hiremath, U. S.; Yelamaggad, C. V.; Rossberg, A. G.; Krishnamurthy, K. S. *J. Phys. Chem. B* **2008**, *112*, 9753.

(23) Kumar, P.; Hiremath, U. S.; Yelamaggad, C. V.; Rossberg, A. G.; Krishnamurthy, K. S. *J. Phys. Chem. B* **2008**, *112*, L9270.

(24) Stannarius, R.; Heuer, J. *Eur. Phys. J. E* **2007**, *24*, 27.

(25) Heuer, J.; Stannarius, R.; Tamba, M. G.; Weissflog, W. *Phys. Rev. E* **2008**, *77*, 056206.

(26) Tadapatri, P.; Hiremath, U. S.; Yelamaggad, C. V.; Krishnamurthy, K. S. *J. Phys. Chem. B* Submitted for publication.

(27) (a) Mauguin, C. *Bull. Soc. Fr. Min.* **1911**, *34*, 71. (b) Gooch, C. H.; Tarry, H. A. *J. Phys. D: Appl. Phys.* **1975**, *8*, 1575.

(28) Penz, P. A. *Phys. Rev. Lett.* **1970**, *25*, 1405.

(29) Carroll, T. O. *J. Appl. Phys.* **1972**, *43*, 1342.

(30) (a) Goscianski, M. *Philips Res. Rep.* **1975**, *30*, 37. (b) Goscianski, M.; Leger, L. *J. Phys. (Paris)* **1975**, *36*, C1–231.

(31) Blinov, L. M.; Barnik, M. I.; Lazareva, V. T.; Trufanov, A. N. *J. Phys. (Paris)* **1979**, *40*, C3–263.

(32) Tikhomirova, N. A.; Ginzberg, A. V.; Kirsanov, E. A.; Bobyshev, Yu. P.; Pikin, S. A.; Adomenas, P. V. *JETP Lett.* **1977**, *24*, 269.

(33) Petrov, M.; Simova, P. In *Forschungen über flüssige Kristalle*; Demus, D., Ed., Martin-Luther-Universatät Halle-Winttenberg: Halle, 1983.

(34) (a) Madhusudana, N. V.; Raghunathan, V. A. *Liq. Cryst.* **1989**, *5*, 1789. (b) Thom, W.; Zimmermann, W.; Kramer, L. *Liq. Cryst.* **1989**, *4*, 309.

(35) Kai, S.; Hirakawa, K. *Solid State Commun.* **1976**, *18*, 1573.

(36) Petrescu, P.; Giurgea, M. *Phys. Lett. A* **1976**, *59*, 41.

(37) Trufanov, A. N.; Blinov, L. M.; Barnik, M. *Sov. Phys. JETP* **1980**, *51*, 314.

(38) Pikin, S. A.; Chigrinov, V. G. *Sov. Phys. JETP* **1980**, *51*, 123.

(39) Pleiner, H.; Brand, H. R. In *Pattern Formation in Liquid Crystals*; Buka, A., Kramer, L., Eds.; Springer: Berlin, 1996.

(40) Rossberg, A. G. *The Amplitude Formalism for Pattern-Forming Systems with Spontaneously Broken Isotropy and Some Applications.* Dissertation, University Bayreuth, 1997; http://wwww.rossberg.net/ag/dissertation.

(41) (a) Huh, J.-H.; Hidaka, Y.; Rossberg, A. G.; Kai, S. *Phys. Rev. E* **2000**, *61*, 2769. (b) Huh, J.-H.; Yusuf, Y.; Hidaka, Y.; Kai, S. *Phys. Rev. E* **2002**, *66*, 031705.

(42) The effective material parameters in eq 1, as given in ref 6, for $p = 0$ are as follows: $k^* = k_{11} + k_{33}q^2$, $\varepsilon_a^* = \varepsilon_a (1 + q^2)(\Sigma^{-1} + \omega'^2 D^{-1})/(1 + \omega'^2)$, $\sigma_a^* = \sigma_a[(D/\Sigma) - (\varepsilon_a\sigma_\perp)/(\varepsilon_\perp\sigma_a)]/(1 + \omega'^2)$, and $\eta^* \approx \eta_1 + (\eta_1 + \eta_2 + \alpha_1)/q^2$, with $\Sigma = 1 + q^2(\sigma_\parallel/\sigma_\perp)$, $D = 1 + q^2(\varepsilon_\parallel/\varepsilon_\perp)$, $\omega' = \omega\tau_q D/\Sigma$, and the wave vector q in units of π/d. The physical constants required for calculation of $|\alpha_2|/\eta^*$ are taken from the experimental data in ref 26.

(43) (a) de Jeu, W. H.; Gerritsma, C. J.; van Zanten, P.; Goossens, W. J. A. *Phys. Lett.* **1972**, *39A*, 355. (b) de Jeu, W. H.; Lathouwers, Th. W. *Mol. Cryst. Liq. Cryst.* **1974**, *26*, 335. (c) Goossens, W. J. A. *Phys. Lett.* **1972**, *40A*, 95. (d) Gerber, P. R. *J. Phys. (Paris)* **1985**, *46*, 1865. (e) Chigrinov, V. G.; Korkishko, T. V.; Barnik, M. I.; Trufanov, A. N. *Mol. Cryst. Liq. Cryst.* **1985**, *129*, 285. (f) Chigrinov, V. G.; Sparavigna, A.; Strigazzi, A. *Phys. Rev. E* **1996**, *53*, 4918.

(44) Nehring, J. *Phys. Rev. A* **1973**, *7*, 1737.

(45) de Gennes, P. G.; Prost, J. *The Physics of Liquid Crystals*; Clarendon Press: Oxford, 1998.

(46) (a) Rossberg, A. G.; Eber, N.; Buka, A.; Kramer, L. *Phys. Rev. E* **2000**, *61*, R25. (b) Eber, N.; Rossberg, A. G.; Buka, A.; Kramer, L. *Mol. Cryst. Liq. Cryst.* **2000**, *351*, 161.

(47) Joets, A.; Ribotta, R. In *Cellular Structures in Instabilities*; Wesfreid, J. E., Zaleski, S., Eds.; Springer-Verlag: Berlin, 1984.

(48) Takeuchi, K. A.; Kuroda, M.; Chate, H.; Sano, M. *Phys. Rev. E* **2009**, *80*, 051116.